Propeller tip vortex mitigation by roughness application

Applied Ocean Research xxx (xxxx) xxx

Contents lists available at ScienceDirect

Applied Ocean Research

journal homepage: www.elsevier.com/locate/apor

Propeller tip vortex mitigation by roughness application

Abolfazl Asnaghi [a], Urban Svennberg [b], Robert Gustafsson [b], Rickard E. Bensow [*,a]

[a] Department of Mechanics and Maritime Sciences, Chalmers University of Technology, Gothenburg 41296, Sweden
[b] Kongsberg Hydrodynamic Research Centre, Kongsberg Maritime Sweden AB, Kristinehamn 68195, Sweden

ARTICLE INFO

Keywords:
Tip vortex
Mitigation
Roughness
Propeller
CFD

ABSTRACT

In this study, the application of surface roughness on model and full scale marine propellers in order to mitigate tip vortex cavitation is evaluated. To model the turbulence, SST $k-\omega$ model along with a curvature correction is employed to simulate the flow on an appropriate grid resolution for tip vortex propagation, at least 32 cells per vortex diameter according to our previous guidelines. The effect of roughness is modelled by modified wall functions. The analysis focuses on two types of vortices appearing on marine propellers: tip vortices developing in lower advance ratio numbers and leading edge tip vortices developing in higher advance ratio numbers. It is shown that as the origin and formation of these two types of vortices differ, different roughness patterns are needed to mitigate them with respect to performance degradation of propeller performance. Our findings clarify that the combination of having roughness on the blade tip and a limited area on the leading edge is the optimum roughness pattern where a reasonable balance between tip vortex cavitation mitigation and performance degradation can be achieved. This pattern in model scale condition leads to an average TVC mitigation of 37% with an average performance degradation of 1.8% while in full scale condition an average TVC mitigation of 22% and performance degradation of 1.4% are obtained.

1. Introduction

A hydrodynamically optimum propeller design usually does not have an optimum hydroacoustic performance as their design restrictions are contradictory (Sezen et al., 2016). This has even further importance for low-noise propellers as their operating profile requires very low radiated noise emissions mostly generated by cavitation (Kuiper, 1981). Tip vortex cavitation (TVC) is usually the first type of cavitation that appears on a propeller, and consequently plays a key role in initiating an overall increasing sound pressure level, and determining the underwater radiated noise (Arndt et al., 2015; Bosschers, 2018). The radiated noise is of big importance because it can disturb marine wildlife and reduces comfort of people on board ship. Therefore, TVC is considered as the main cavitation characteristics to control in the design procedure.

The blade load distribution is a decisive parameter in the tip vortex cavitation formation (Kuiper, 2001). With a highly loaded tip, vorticity is generated at the trailing edge of a propeller blade, resulting in a stable trailing vortex formation. With reduced tip loading, separation still occurs close to the tip, while the trailing vortex is much weaker, leading to a local tip vortex formation typical for a standard ship propeller. An unloaded tip design forces the loading towards inner radii and at these inner radii, leading edge separation, and therefore a leading edge vortex, may be formed and the trailing vortices become more evenly distributed (Long et al., 2020; Lu et al., 2014). In this condition, effects of non-uniform flow field (Korkut and Atlar, 2002; Pereira et al., 2016), and blade surface roughness (Dreyer, 2015; Felli and Falchi, 2011) should also be considered.

The start of cavitation in the tip vortex, TVC inception (TVCI), determines a break point where nuisance suddenly increases. Cavitation will occur in the core of a tip vortex only if a nucleus has enough time to reach the core and then triggers cavitation (Boulon et al., 1997). It is well reported that cavitating behaviour of a tip vortex depends on the nuclei radius, its initial location, vortex circulation, and vortex velocity (Arndt and Keller, 1992; Brianon-Marjollet and Merle, 1997; Hsu, 1991; Ligneul and Latorre, 1993). Depending on the water quality, TVCI can be either a sudden appearance of a continuous cavity, or an intermittent appearance of an elongated bubble extending axially over a relatively small portion of the tip vortex (Higuchi et al., 1989; Maines and Arndt, 1997). At the intermittent step, formation and collapse of elongated bubbles increase noise intensity significantly compared with the fully developed TVC (Pennings et al., 2015). Looking at vortex singing, the tones are very different under different flow conditions and water

* Corresponding author.
E-mail address: rickard.bensow@chalmers.se (R.E. Bensow).

https://doi.org/10.1016/j.apor.2020.102449
Received 3 July 2020; Received in revised form 20 October 2020; Accepted 9 November 2020

quality where the vortex singing can only exist in the transferring process between strong tip vortex cavitation and weak tip vortex cavitation (Peng et al., 2017; 2015).

Traditional potential flow propeller design tools, in connection with designer experience, are able to provide optimal geometries in terms of efficiency, and to some extent capture the effects of on-blade cavitation, but they are not suited for the assessment of negative aspects of cavitating tip vortices. Apart from redesigning a propeller to redistribute load and consequently changing TVC properties (Shin and Andersen, 2015), a few approaches has been proposed to suppress TVC, classified as active control and passive control methods. In active control approaches, the tip vortex flow is altered by injection of a solution, e.g. air (Rivetti et al., 2014), polymer (Fruman and Aflalo, 1989; Ryo, 2009), or water (Chahine et al., 1993; Chang et al., 2011), into the tip vortex region. In passive control methods, the boundary layer and momentum distribution around the blade tip are altered aiming to weaken the tip vortex and its nuclei capture capability. Inclusion of an extra geometry on the blade tip (Brown et al., 2015; Gim and Lee, 2013; Park et al., 2014), drilling holes on the blade (Aktas et al., 2019), and roughening the blade surface (Asnaghi et al., 2019c; Johnsson and Ruttgerson, 1991; Kruger et al., 2016; Souders and Platzer, 1981) are some examples of passive TVC mitigation, of which the latter is the concern of this study.

Surface roughness affects the tip vortex roll-up as roughness elements promote transition to turbulence and growth of laminar boundary layers and thereby alter the near-wall flow structures. The vortical structures generated by the roughness elements interact with the main tip vortex and destabilize it. If size, pattern, and location of roughness elements are selected appropriately, the destabilization process leads to tip vortex breakdown, and consequently to TVC mitigation. This, however, increases the losses and leads to performance degradation (Asnaghi et al., 2019c; Johnsson and Ruttgerson, 1991; Kruger et al., 2016). To minimize this degradation, one has to optimize the roughened area which itself demands a detailed knowledge on where and how the tip vortex is formed. For propellers in behind conditions, this is even more complex as the tip vortex location and origin vary.

In our previous study, the mechanism of tip vortex mitigation due to roughness is investigated on an elliptical foil with focusing on how roughness affects the boundary layer and momentum distribution close to the tip (Asnaghi et al., 2020b). Here, the analysis is extened into marine propellers where different flow properties are analyzed to define effective areas in tip vortex formation and its roll-up. The selected propeller is from a research series of highly skewed marine propellers having a low effective tip load which is typical for yachts and cruise ships. Previously, numerical simulations of tip vortex flows around this propeller having smooth blades have been carried out and successfully compared with experimental measurements (Asnaghi et al., 2018b). The aim of the present study is to provide further knowledge about the effects of the surface roughness on the TVC and the possibility of using roughness to delay the cavitation inception.

The turbulent flow field around the propellers is modelled by using the two-equation SST $k-\omega$ model of OpenFOAM on appropriate grid resolutions for tip vortex propagation, at least 32 cells per vortex diameter according to previous studies guidelines (Asnaghi, 2018; Asnaghi et al., 2019a). To prevent overprediction of turbulent viscosity in highly swirling tip regions, η_3 curvature correction method is employed (Arolla, 2013; Arolla and Durbin, 2014). The roughness is included in the simulations by employing two different approaches. In the first approach, rough wall functions are used to mimic the effects of roughness by modifying the turbulent properties in roughed areas (Tapia, 2009). The second approach modifies the mesh topology by removing cells in roughed areas to create random roughness elements.

To identify the areas where roughness has to be applied, three criteria based on the flow properties of the smooth propeller condition are employed. The Q-criterion is selected to identify the vortical structures and their interactions. The second criterion is the flow streamlines close to the blade surface helping to highlight from which areas on the blade the vortex momentum is provided. The third criterion is the pressure coefficient used to distinguish the areas where the cavitation incepts inside the tip vortex. These criteria are used to find a good roughness pattern that can lead to a proper tip or leading edge vortices mitigation with reasonable performance degradation.

The strategy used to find the suitable roughness pattern in model scale condition is extended to find the roughness pattern in full scale conditions. This has been done by considering the flow properties of the smooth propeller in the full scale condition as well. Then, the best roughness pattern application is evaluated at three operating conditions, i.e. $J = 0.82$, 0.93 and 1.26. Contradictory to the model scale analysis where a rough wall function is employed to incorporate the effects of roughness, in the full scale analysis the roughness elements are included as a part of computational domain. This gives the possibility of resolving the flow around the roughness elements, and also allows to use smaller y^+ for the blade surfaces.

The results contain the performance and cavitation inception charts of the propeller in model and full scale conditions. It is investigated how having different roughness patterns alter vortical structures on the blade and in the tip vortex region. The roughness area is optimized by simultaneous consideration of the tip vortex mitigation, performance degradation and their compromise. The performance and TVC mitigation of the propeller having optimum roughness pattern are discussed.

2. Governing Equations

The OpenFOAM package, used in this study for numerical simulation, is an open source code written in C++ to model and simulate fluid dynamics and continuum mechanics (Ope, 2015). The incompressible conservation of mass and momentum equations are solved using the PIMPLE algorithm, a merge of the SIMPLE and PISO algorithms. The solver has been used and validated for various marine applications including cavitation and tip vortex analysis; see (Asnaghi, 2018; Asnaghi et al., 2020a; Bensow, 2011; Bensow and Bark, 2010) for more details on the modelling and the numerical setup used in OpenFOAM.

2.1. Turbulence model

The turbulence is modelled by employing the SST $k-\omega$ model along with a curvature correction (CC) model (Asnaghi et al., 2019a). In the selected model, the production term of the ω equation is multiplied by F_{rc},

$$F_{rc} = 1 + \alpha_1|\eta_3| + 3\alpha_1\eta_3, \tag{1}$$

where $\alpha_1 = -0.2$ and $C_r = 2.0$. In this equation, η_3 is a velocity gradient invariants defined through the non-dimensional strain rate and rotational rate tensors (Arolla, 2013),

$$\eta_1 = \overline{S}^*_{ij}\overline{S}^*_{ij}, \quad \eta_2 = \overline{\Omega}^*_{ij}\overline{\Omega}^*_{ij}, \quad \eta_3 = \eta_1 - \eta_2, \tag{2}$$

$$\overline{S}^*_{ij} = \tau\overline{S}_{ij}, \quad \overline{\Omega}^*_{ij} = \tau\overline{\Omega}^{mod}_{ij}, \tag{3}$$

where the strain rate and rotational rate tensors are defined by,

$$\overline{S}_{ij} = \frac{1}{2}\left(\frac{\partial\overline{u}_i}{\partial x_j} + \frac{\partial\overline{u}_j}{\partial x_i}\right), \quad \overline{\Omega}_{ij} = \frac{1}{2}\left(\frac{\partial\overline{u}_i}{\partial x_j} - \frac{\partial\overline{u}_j}{\partial x_i}\right). \tag{4}$$

As can be seen, η_1 represents the non-dimensional strain rate magnitude, η_2 represents the non-dimensional vorticity magnitude, and η_3 is a linear combination of these two velocity-gradient invariants. The turbulent time scale used to non-dimensionalize these tensors is calculated by (Arolla, 2013; Arolla and Durbin, 2014; StarCCM, 2017),

$$\tau = \max(\tau_1, \tau_3), \quad \tau_1 = \frac{1}{\beta^*\omega}, \quad \tau_2 = 6\sqrt{\frac{\nu}{\beta^* k\omega}}, \quad \tau_3 = \left(\tau_1^n\tau_2\right)^{\frac{1}{n+1}}, \tag{5}$$

where $n = 1.625$. The time scale is limited in order to have a correct near-wall asymptotic behaviour.

The modified rotational rate tensor incorporating the streamline curvature and frame rotation is,

$$\overline{\Omega}_{ij}^{mod} = \overline{\Omega}_{ij} + \Omega_{ij}^{F} + (C_r - 1)W_{ij}^{A}, \tag{6}$$

where C_r is the constant of the equation and depends on the CC model (Arolla, 2013). This coefficient takes a value of 2 for bifurcation approaches. Here, Ω_{ij}^{F} represents the frame rotational tensor calculated from $\Omega_{ij}^{F} = -\epsilon_{ijk}\Omega_{k}^{F}$ where Ω_{k}^{F} is the angular frame velocity about the x_k-axis. The W_{ij}^{A} tensor which contains the effects of curvature corrections in the rotational rate tensor is defined by Wallin and Johansson (2002),

$$W_{ij}^{A} = -\epsilon_{ijk}B_{km}\overline{S}_{pr}\frac{D\overline{S}_{rq}}{Dt}\epsilon_{pqm}, \tag{7}$$

$$B_{km} = \frac{II_S^2\delta_{km} + 12III_S\overline{S}_{km} + 6II_S\overline{S}_{kl}\overline{S}_{lm}}{2II_S^3 - 12III_S^2}, \tag{8}$$

$$II_S = \overline{S}_{kl}\overline{S}_{lk}, \quad III_S = \overline{S}_{kl}\overline{S}_{lm}\overline{S}_{mk}, \tag{9}$$

where $\frac{D\overline{S}_{rq}}{Dt}$ is the material derivative of the strain rate tensor. Please refer to (Arolla, 2013; Asnaghi, 2018) for further information.

2.2. Roughness modelling

The flow around the roughness elements can be either resolved or modelled. To resolve the flow, roughness geometries have to be included into the computational domain which leads to having finer cell resolution around them compared to the rest of the domain, and consequently demands for higher computational resources. Modelling roughness elements requires much lower number of computational cells but as it involves simplification of the roughness geometry, the flow physics may not be correctly modelled.

In the current study for modelling roughness elements, the wall function developed by Tapia (2009) for the inner region of the turbulent boundary layer or the log-law region (e.g. $11 \leq y^+$ in OpenFOAM wall functions) is used,

$$u^+ = \frac{1}{\kappa}\ln(Ey^+) - \Delta B, \tag{10}$$

with the von Karman constant $\kappa = 0.41$, the constant E=9.8, the dimensionless wall distance $y^+ = u_\tau y/\nu$, and the velocity shift correction ΔB due to the roughness elements. In this model, the nondimensional roughness height is presented by $K_s^+ = u_\tau K_s/\nu$ where K_s is the roughness height, $u_\tau = \sqrt{\tau_w/\rho}$ is the shear velocity, and τ_w is the wall shear stress. As this model only affects the viscosity of the first cell adjacent to the wall, the height of the roughness elements should be smaller than the height of the cells wall normal distance, i.e. $K_s^+ \leq y_w^+$. Otherwise, the part of roughness elements that locates outside the adjacent cells will not be included in the modelling.

The flow regime over a rough surface depends on how roughness elements interact with different parts of the boundary layer. If the roughness elements are embedded in the viscous sublayer, the friction drag is not affected by the roughness and the flow regime is smooth. In a smooth regime represented by $K_s^+ \leq 2.5$, the correction ΔB is set to zero and the wall function recalls the smooth wall function.

In the case where the roughness element heights are much larger than the boundary layer thickness, the fully rough regime forms where the drag significantly increases. In such a condition, the pressure drag on the roughness elements dominates and the impact of roughness becomes independent of Reynolds number which means the viscous effect is no longer important. For a fully rough regime represented by $90 \leq K_s^+$, the ΔB correction is represented by,

$$\Delta B = \frac{1}{\kappa}\ln\left[1 + C_s K_s^+\right] \tag{11}$$

The transition regime happens where both viscous and pressure forces on the roughness elements contribute to the wall skin friction. In this condition represented by $2.5 < K_s^+ < 90$, the correction reads,

$$\Delta B = \frac{1}{\kappa}\ln\left[\frac{K_s^+ - 2.25}{87.75} + C_s K_s^+\right]\sin\left(0.425\left[\ln\left(K_s^+\right) - 0.811\right]\right) \tag{12}$$

In these equations, shape and form of roughness elements are incorporated into the modelling through the C_s coefficient. However, there is no clear guideline to adjust this coefficient. It is suggested that it varies from 0.5 to 1 where $C_s = 0.5$ corresponds to the uniformly distributed sand grain roughness. If the roughness elements deviate from the sand grains, the constant roughness should be adjusted by comparing the results with experimental data.

2.3. Parameters defining the flow properties

The hydrodynamic performance of a propeller is defined by using the non-dimensional thrust and torque coefficients, and the advance ratio,

$$K_T = \frac{T}{\rho n^2 D^4}, \quad K_Q = \frac{Q}{\rho n^2 D^5}, \quad J = \frac{V_A}{nD}, \tag{13}$$

where D is the propeller diameter, n is the rotational speed of the propeller in rev/sec, ρ is the fluid density, T is the propeller thrust force, Q is the propeller shaft torque, and V_A is the mean inflow velocity towards the propeller plane. In the current study, the inlet velocity is kept constant and then the advance ratio is set by adjusting the propeller rotational speed, i.e. n.

To identify vortical structures in the flow, the Q-criterion representing the local balance between shear strain and rotational tensor magnitudes, is employed (Hunt et al., 1998; Kolar, 2007),

$$Q = \frac{1}{2}\left(\overline{\Omega}_{ij}\overline{\Omega}_{ij} - \overline{S}_{ij}\overline{S}_{ij}\right). \tag{14}$$

To simplify the cavitation inception detection, the minimum pressure criterion is employed (Asnaghi et al., 2018b). The criterion assumes that cavitation occurs as soon as the minimum pressure in the flow reaches the saturation pressure. Therefore, the cavitation inception point, σ_i, is determined from the pressure field of the wet flow as,

$$\sigma_i = -C_{p,\min}. \tag{15}$$

This simple indicator can be used to compare and evaluate the tip vortex strength in the smooth and roughened propellers. However, it cannot provide information on how the nuclei capture property of a tip vortex changes in different conditions. This may not be an issue in the full scale operations where it is known that water is filled with nuclei, i.g. weak water, but for the model scale applications where nuclei distribution has a greater impact on the tip vortex inception the nuclei capture property can be useful to evaluate the involving mechanisms. This demands more advance models with the capability of tracking nuclei, e.g. (Ghahramani, 2020; Ghahramani et al., 2019), or perhaps with the capability of non-condensable gas inclusion as a part of the analysis (Cheng et al., 2021).

3. Case description

The basic design of the propeller is from a research series of five-bladed highly skewed propellers having low effective tip load for vessels where it is very important to suppress and limit propeller-induced

vibration and noise. The main, or first occuring source of noise, for this type of propellers, is cavitation in the tip region. In the previous studies conducted by the authors (Asnaghi, 2018; Asnaghi et al., 2018b; 2020a), the computational guideline to successfully model the tip vortex flow around this propeller having smooth surface within OpenFOAM was investigated. In this guideline, the turbulence modelling impact, minimum required spatial mesh resolution for modelling the tip vortex in the near field region and the numerical set up that can provide low numerical dissipation and high stability are discussed. Here, the same guideline for the computational domain and mesh specifications is employed.

The computational meshes were generated by StarCCM+ and then converted into the OpenFOAM format. As the open water conditions was of interest, simulation of the flow around one blade and then using cyclic boundaries on the sides were possible. However, when the numerical analysis of the model scale propeller was conducted, there were some stability issues with the cyclic boundaries making it very cumbersome to converge. Therefore, the whole propeller is modelled and in order to keep the number of cells low enough, the tip vortex refinement was applied on one blade only. The utility used to convert StarCCM+ mesh to the OpenFOAM format has a limitation on the number of cells or faces which forced using the Trimmer mesher to create the model scale propeller mesh. For the full scale propeller, using the Trimmer mesher led to some bad quality cells, e.g. wrongly oriented faces or face non-orthogonality more than 85 degrees. This problem is believed to be related to the low numerical precision of reading or writing the points storing the locations of cells and faces. However, during the study it was not possible to find out where this low reading or writing precision occurs. At the same time as we were able to improve the stability of employing cyclic boundaries, the polyhedral mesher is used to create the mesh around the full scale blade.

The computational domain used for the model scale propeller is presented in Fig. 1(a). The domain is simplified to a cylinder extending 4D upstream the propeller and 8D downstream of the propeller where $D = 0.2543$ m is the diameter of the propeller. The simulations are conducted at a constant inlet velocity, a fixed pressure outlet boundary and the advance ratio of the propeller is then set by adjusting the rotational rate of the propeller. No-slip wall boundary condition is used for the propeller and the shaft. The outer cylinder boundary is set as a slip boundary to reduce the mesh resolution requirements far from the propeller. Then, in order to consider the blockage effects, the numerical results are compared against the experimental measurements which would provide the same velocity at the cavitation tunnel measurement point. In order to model the moving mesh (i.e. relative motion between the propeller and the external domain), the computational domain has been decomposed into two regions connected to each other through AMI (Arbitrary Mesh Interpolation) boundaries (Asnaghi et al., 2015). While the outer region is stationary, the rotation of the region close to the propeller where all interesting flow phenomena occur has been handled by MRF.

Different refinement boxes are applied to provide finer resolutions around the rotating propeller region, Fig. 1(b). The baseline mesh resolution on the blades gives x^+ and $z^+ < 250$, with much finer resolutions at the leading edge and trailing edge of the blades due to the high geometry curvature. Here, x^+ and z^+ are non-dimensionalized resolutions in x and z directions calculated similar to y^+ term, i.e. $x^+ = u_\tau \Delta x/\nu$ and $z^+ = u_\tau \Delta z/\nu$. In these definitions, Δx and Δz are the cell resolution in x and z directions, respectively. As the surface resolution close to the tip is determined by the tip refinement boxes, even finer resolution is achieved at the blade tip and the leading edge. The prismatic layers of the refined blade consists of 20 layers having extrusion factor of 1.15 where the first cell wall normal resolution is set equal to $y^+ = 35$ for wall modelling simulations, and equal to $y^+ = 5$ for resolving the flow around the roughness elements. It should be noted that when generating the computation grids, an estimation of y^+ is used to define the first cell normal resolution. However, during the simulations as the wall shear velocity, u_τ, is computed based on the flow properties, the actual value of y^+ changes.

As mentioned, the tip vortex refinement is applied on one blade only where three helical shape refinement zones are defined based on the primary vortex trajectory. The refinement zones cover the tip of the

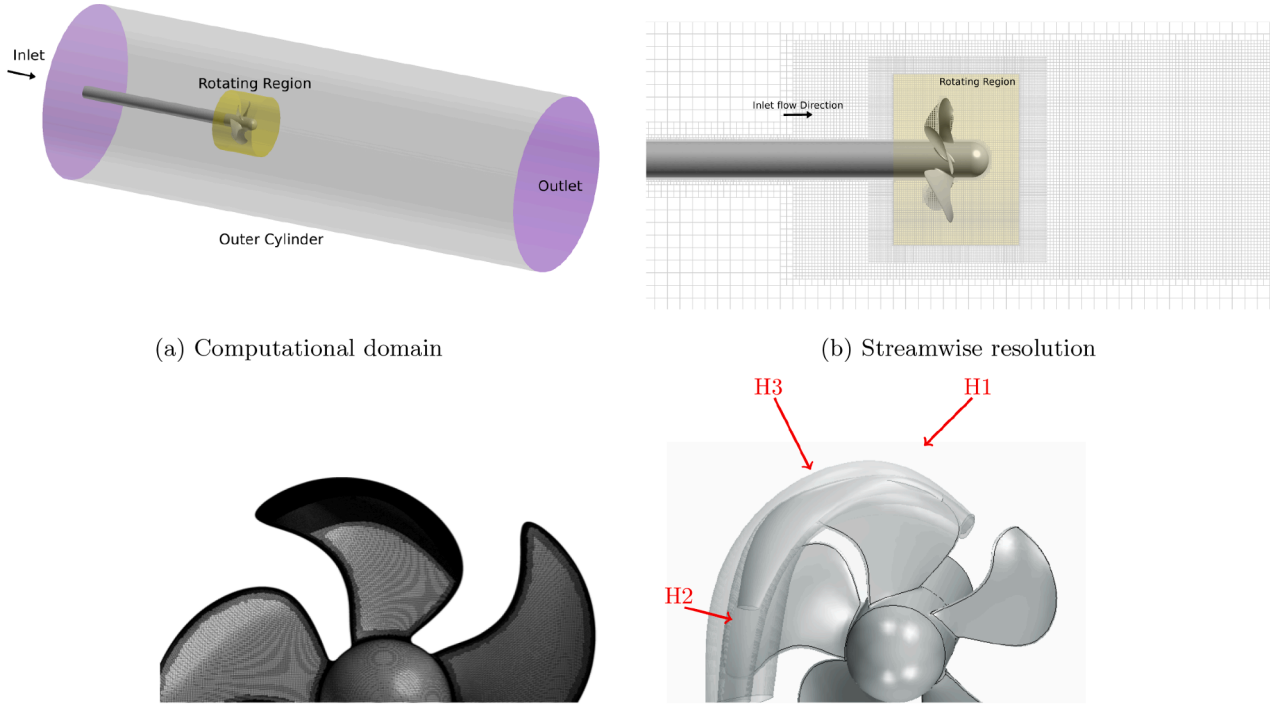

(a) Computational domain

(b) Streamwise resolution

(c) Blade surface resolution

(d) Helical tip refinement

Fig. 1. Mesh distribution of the model scale propeller.

blade, and therefore provide more refined grid resolutions on the tip of this blade, Fig. 1(c). These helical refinement regions provide spatial resolutions as fine as 0.2 mm, 0.1 mm, and 0.05 mm in H1, H2, and H3 regions for the model scale propeller mesh, respectively.

The full scale propeller is constructed by the geometrical scale ratio of 15 from the model scale propeller leading to the propeller diameter of 3.8145 m. As noted earlier, the computational domain of the full scale propeller consists of one blade and cyclic boundaries on the sides, Fig. 2. Similar to the model scale settings, the cells are clustered towards the rotating region. The tip vortex refinements follow the same strategy where three helical refinement regions defined based on the primary vortex trajectory are considered around the blade tip to specify the desired resolution at this region.

In Table 1, the operating conditions and normalised resolution details of the blade and tip vortex refinements are presented. As mentioned earlier, the inlet velocity is kept constant in all of the simulations while the propeller rotational speed is adjusted to achieve the desired propeller advance ratio. Similar to the propeller surface resolution, the tip vortex refinement resolutions are presented by the non-dimensionalized terms, i.e. $H_1^+ = u_\tau \Delta H_1/\nu$, $H_2^+ = u_\tau \Delta H_2/\nu$ and $H_3^+ = u_\tau \Delta H_3/\nu$. In these equations, ΔH_1, ΔH_2 and ΔH_3 are the specified cell resolutions in the helical tip refinement regions of H1, H2 and H3. As stated in this table, the mesh number and its distribution in model scale and full scale simulations are different. In each condition, the baseline blade surface resolution, i.e. x^+ and z^+, is selected according to our previous studies and also the computational cost we could afford. The wall normal resolution, y^+, is selected according to the roughness modelling strategy. In both model scale and full scale conditions, we have used three helical refinement regions defined based on a primary tip vortex trajectory obtained through an initial simulation on a coarser mesh resolution. Therefore, as the tip vortex trajectory may differ in model scale and full scale conditions, the refinement geometries also differ in these conditions. Their grid resolutions, H^+, also differ and depends on the estimation of tip vortex radius and also on the computational cost we could afford.

Based on our previous studies for mitigation of back side tip vortices (Asnaghi et al., 2019b; 2019c), the tip region of the refined blade, Fig. 3, is considered the starting point to investigate the roughness impact on for wider operating conditions. The roughness areas highlighted in Fig. 3 are thus selected based on the flow properties of tip vortices that incept on the tip or slightly downstream. For the propeller design considered in this study, this type of vortices is observed at low advance ratio numbers, e.g. $J = 0.82$.

The study consist of the roughness modelling on the blade tip sides, i.e. the back side and the Front side. For one case where the roughness is only applied on the back side tip region, BS Tip, the mesh topology is modified by removing cells to include the roughness elements into the simulations, Fig. 3(c). This will provide the opportunity to resolve the flow around these roughness elements.

At higher J values, e.g. $J = 1.26$, the main vortex appears as a leading edge vortex formed on the front side of the blade, and it is thus expected the area covered with roughness is different. Therefore, the roughness pattern optimization for this vortex consists of investigation of radial areas defined in Fig. 4(a). In order to find which part of radial areas will have more impact on TV mitigation, also smaller areas along the leading edge are considered, e.g. as in Fig. 4(b). The summary of evaluated roughness patterns and arrangements are presented in Table 2.

Following our previous studies (Asnaghi et al., 2019b; 2019c), all of the analysis is performed by considering a fixed value for the roughness height, $K_s = 250$ μm in model scale condition; this corresponds to $K_s^+ = 35$. The roughness height is extended into the full scale condition by considering the geometrical scale ratio. This gives $K_s = 3.75$ mm in full scale conditions corresponding to $K_s^+ \approx 925$.

In Fig. 5, the close-up view of the roughness elements employed in the full scale propeller simulations is presented. As can be seen, the normal resolution applied to each roughness element is quite satisfactory, and each elements contains at least 20 grid points in the normal direction. The surface resolution, however, is limited by the finest tip vortex refinement we could afford, i.e. $H_3^+ = 150$.

4. Results

Open water performance of the propeller in the model scale and full scale conditions are presented in Fig. 6. The figure includes thrust coefficient, K_T, torque coefficient, K_Q, and efficiency, η_0, at different advance ratio values, J. The model scale results are presented by solid lines while the full scale results are shown by dashed lines.

General accuracy of the results is satisfactory and agrees well with the experimental measurements. The trend in the forces, however, are predicted differently in model and full scales. In $J < 1.1$, the thrust and torque coefficients of the full scale condition are predicted higher than the model scale predictions. This is found to make a small difference on the predicted efficiency in this range as the increase of both coefficients cancels each other. In higher J values, i.e. $1.1 < J$, the trend of thrust and torque predictions between model scale and full scale switches where both of forces are underpredicted in the full scale condition, although this is more apparent for the thrust. This leads to predictions of lower efficiency in full scale compared to the model scale results. The cavitation inception prediction of the propeller for the model scale and full scale conditions are presented in Fig. 7. Three different cavitation types are investigated: FTV, front tip vortex; BTV, back tip vortex; and BBC, back bubble cavitation. In this figure, the experimental measurements are presented by solid circular symbols while numerical results predicted by the minimum pressure criterion is presented by triangular symbols. In order to provide further data for analysis, the experimental measurements are extrapolated to the sides of the chart, presented by solid lines.

The overall comparison in model scale is quite satisfactory, with BTV well predicted and BBC only somewhat smaller inception values, while the FTV shows larger discrepancies; however the minimum point in the bucket diagram is well captured. Comparison of the model scale and full scale results indicate a stronger back side tip vortex and bubble cavitation predictions in the full scale condition. The prediction of the front side tip vortex is found to be opposite where a stronger front tip vortex is

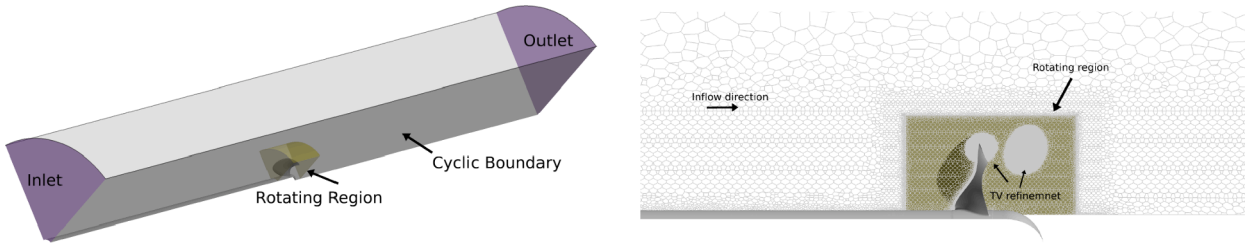

(a) Computational domain (b) Streamwise resolution

Fig. 2. Mesh distribution of the full scale propeller.

Table 1
Operating conditions and mesh specifications of the propeller in model scale (MS) and full scale (FS) conditions.

	Propeller setup			Blade resolution			TV resolution			Total number of cells (M)
	D(m)	U_{in} (m/s)	Re	y^+	x^+, z^+ baseline	x^+, z^+ refined tip	$H1^+$	$H2^+$	$H3^+$	
MS	0.2543	4.2	1.07×10^6	5 and 35	250	10	40	20	10	87.3 and 87.1
FS	3.8145	8	30.5×10^6	50	5000	150	600	300	150	37.3

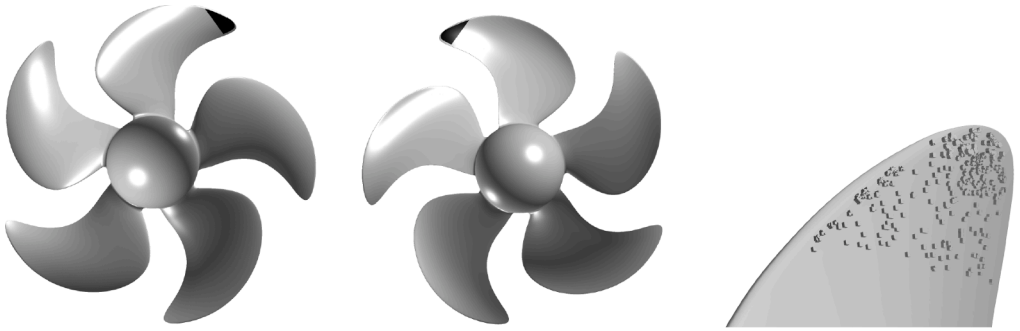

(a) Back side view (b) Front side view (c) Geometrical roughness

Fig. 3. (a) and (b): Roughness areas coloured black on the back side and front side of the refined blade; (c): zoomed view of the roughness elements inclusion.

Table 2
Summary of the roughness patterns tested on the back and front sides of the blade.

Pattern	Where the roughness is applied:	Related figure
Smooth	The blade is smooth.	–
FS	Front side of the blade	
BS	Back side of the blade	
FR	Both sides of the blade (fully roughened)	
BS Tip	Back side tip	Fig. 3(a)
FS Tip	Front side tip	Fig. 3(b)
BS + FS Tip	Tip of the back and front sides	Fig. 3(a) and (b)
R7080	Radial distance $0.7 < r/R < 0.8$ on the front side	Fig. 4(a)
R8090	Radial distance $0.8 < r/R < 0.9$ on the front side	
R90100	Radial distance $0.9 < r/R < 1.0$ on the front side	
R70100	Radial distance $0.7 < r/R < 1.0$ on the front side	
RE8090	Leading edge on the radial distance $0.8 < r/R < 0.9$ of the front side	Fig. 4(b)
RE8595	Leading edge on the radial distance $0.85 < r/R < 0.95$ of the front side	
RE90100	Leading edge on the radial distance $0.9 < r/R < 1.0$ of the front side	
RE80100	Leading edge on the radial distance $0.8 < r/R < 1.0$ of the front side	
ORP	Optimum roughness pattern = combination of BS Tip and RE80100	Figs. 3(a) and 4(b)

observed in the model scale condition.

4.1. Flow properties of model scale propeller

The flow properties at low J values where the tip vortex forms on the back side of the blade are presented in Fig. 8. In this figure, the tip vortex is presented by the pressure coefficient iso-surface, the flow streamlines are presented by white lines, and the blade surface is coloured by the pressure coefficient distribution.

As expected, at lower J values, which corresponds to higher propeller rotational speeds, the back tip vortex becomes stronger. This corresponds to more concentrated flow streamlines which feed the tip vortex momentum. This can be noted on the back side especially close to the trailing edge in $0.9 < r/R < 0.95$. On the front side, no obvious concentrated streamlines in any region are observed. It seems that the flow streamlines from the front side evenly contribute to the tip vortex roll-up downstream of the tip rather than where the tip vortex starts. This analysis can be extended in the future study by unsteady simulations of the flow to highlight the spatial-temporal development of tip vortex and effective flow regions (Han and Tan, 2019; 2020).

In Fig. 9, distributions of vortical structures at low J values are presented by the iso-surface of Q-criterion equal to 200. The results clearly show that at higher rotational rate, i.e. lower J values, more trailing vortices are formed on the blade close to the trailing edge, especially after the blade mid-chord. More interestingly, in $0.9 < r/R < 1.0$, the vortical structures distinguish a triangular area on the tip which corresponds to the area where concentrated flow streamlines enter.

Based on the flow properties analysis of lower J values, triangular areas on the back side and front side of the blade are considered as effective areas in formation of the back side tip vortex. These areas are presented in Fig. 3.

The flow properties at higher J values where the tip vortex forms as a leading edge vortex are presented in Fig. 10. As expected, by increasing J values, the vortex becomes stronger and incepts at lower radii, e.g. $r/R = 0.7$ at $J = 1.26$. This leads to more flow suction into the rotating vortex region which can be noted from more concentrated flow streamlines on the front side in $r/R < 0.6$. On the blade back side, the flow streamlines indicate a clear separation line distinguished by concentrated streamlines close to the blade trailing edge. The streamlines also highlight how the flow from lower radii moves towards the tip.

Distribution of vortical structures presented in Fig. 11 shows how the leading edge vortex is formed. It is clear that the trailing vortices shed from both back side and front side contribute to the tip vortex structures especially after leaving the blade. However, it is not clear whether this contribution affects the leading edge vortex strength in the region it incepts, i.e. $0.8 < r/R < 0.95$ noted from the pressure iso-surface presented in Fig. 10.

These results clarify the significance of flow structures formed in $0.7 < r/R$ on the vortex strength and its development. Therefore, different roughness arrangements are considered for the front side tip vortex mitigation based on radial distances and pressure distribution, Fig. 4. The summary of these arrangements and their brief descriptions are presented in Table 2.

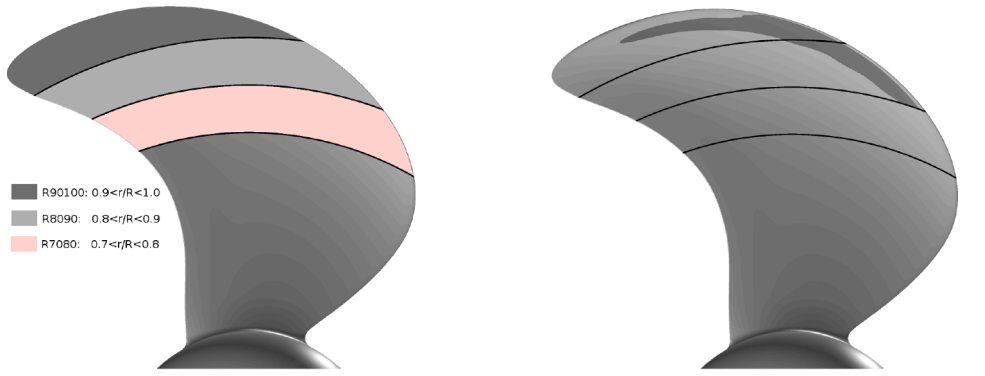

(a) Radial roughness patterns (b) Radial leading edge roughness pattern

Fig. 4. Roughness patterns tested on the front side of the propeller.

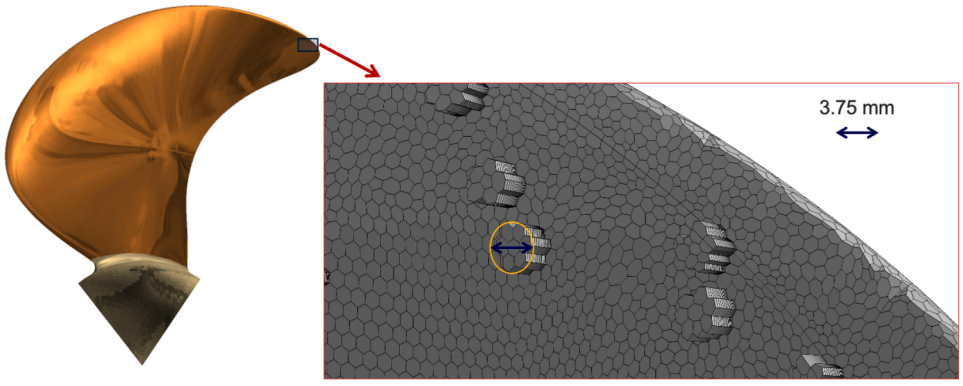

Fig. 5. Close-up view of the roughness elements applied in the propeller full scale simulations.

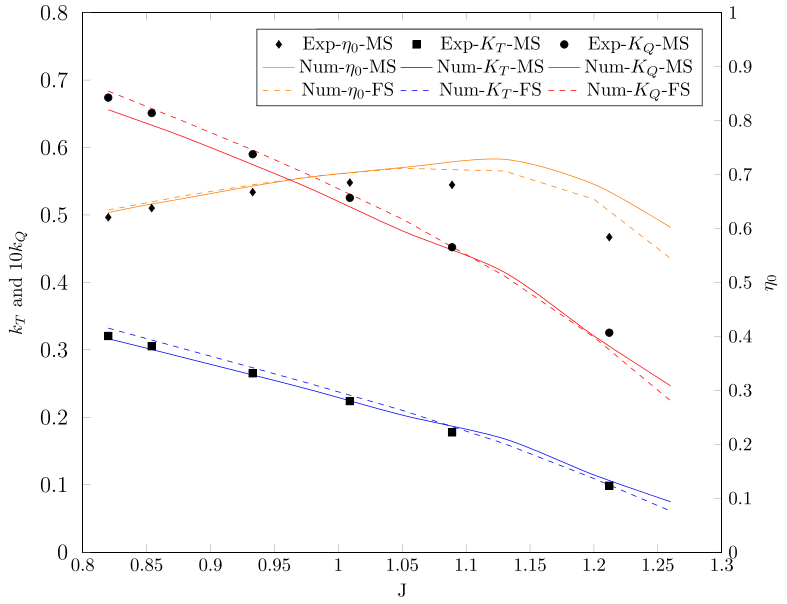

Fig. 6. Open water performance of the smooth propeller in model scale and full scale conditions.

As can be noted from Figs. 8 and 10, different values of C_p are used to present back side and front side tip vortices. This selection corresponds to the tip vortex strength and propeller load in different advance ratio values. In highly loaded propeller, i.e. low J values, tip vortex is stronger and therefore, cavitation incepts earlier than lightly loaded propeller, i. e. higher J values. This can be observed also in Fig. 7 where the cavitation inception chart over different operating conditions is presented.

4.2. Mitigation of back side TVC

Performance of the propeller for different surface roughness condi-

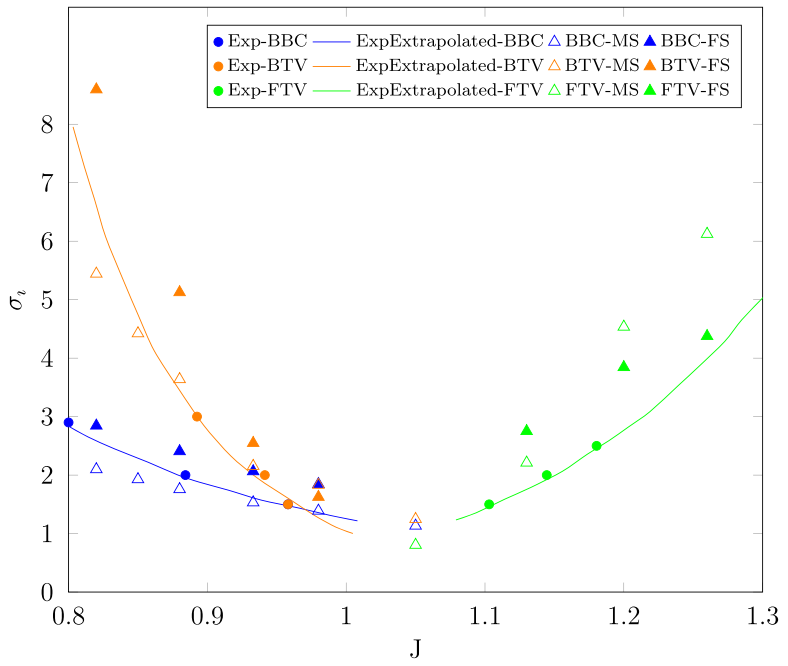

Fig. 7. Open water cavitation inception diagram of the smooth propeller in the model scale (MS) and full scale (FS) conditions represented by FTV: front tip vortex, BTV: back tip vortex, and BBC: back bubble cavitation.

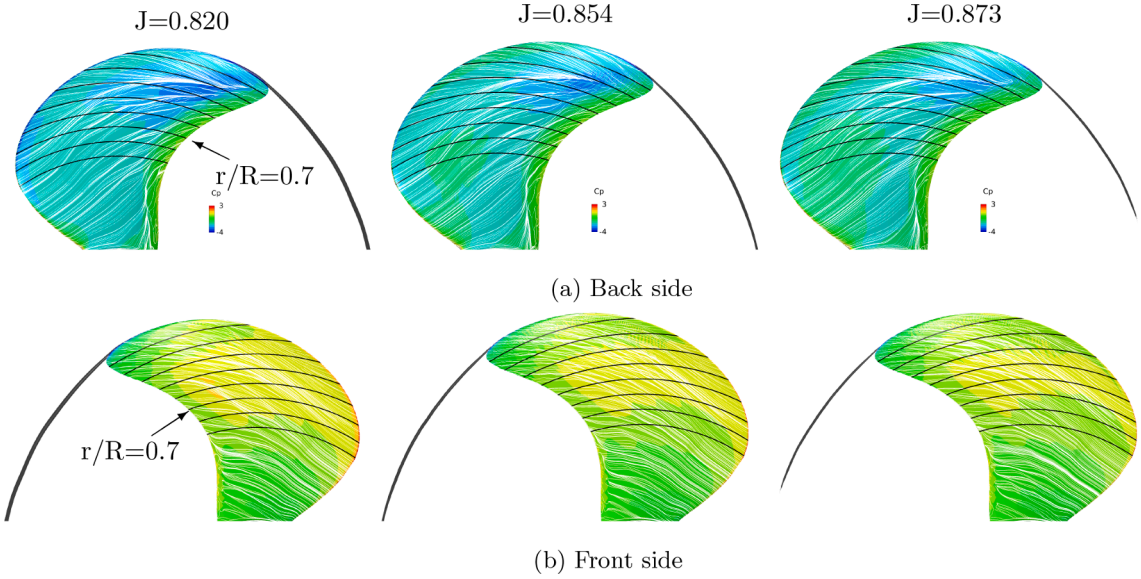

Fig. 8. Flow properties at different back side tip vortex conditions. The blade surface is coloured by C_p distribution, the flow streamlines are presented in white, the tip vortex is presented by the pressure iso-surface equal to $C_p = -4$ coloured in black.

tions are presented in Table 3 where the roughness is modelled via the rough wall function. Thrust and torque coefficients as well as the efficiency are presented relative to the smooth propeller condition at $J = 0.82$ where the tip vortex is formed on the back side. In all of the tested roughness arrangements, the results indicate an increase in the torque coefficient when roughness is included. The thrust coefficient, however, is more dependent on the roughness pattern. For the FR blade, the maximum thrust decrease, $-$ 13.4%, and efficiency drop, $-$ 16.6%, are observed. Having roughness on the FS tip leads to higher K_t but it also requires a higher K_q. This eventually results in a lower propeller efficiency, around $-$ 2.5%. When roughness is only applied on the BS tip, the variation of the thrust and torque is smallest. A true quantitative justification of these results demands uncertainty analysis, but it is anticipated that the trends are correctly capture at this grid refinement level. The results, however, clearly confirm that in order to minimise the negative effects of roughness on the propeller performance, the roughness area should be optimised.

In Fig. 12, the predicted cavitation inception based on the minimum pressure criterion is presented for different roughness patterns defined for the back side TVC at $J = 0.82$. As the propeller was not tested at this operating condition, the experimental data is extrapolated to this condition. As expected, the FR condition has the lowest cavitation inception compared to other roughness patterns. The predicted cavitation inception in the BS tip and BS+FS tip patterns is close to each other, and the difference between them is believed to lie in the uncertainty of the numerical results in the current simulations.

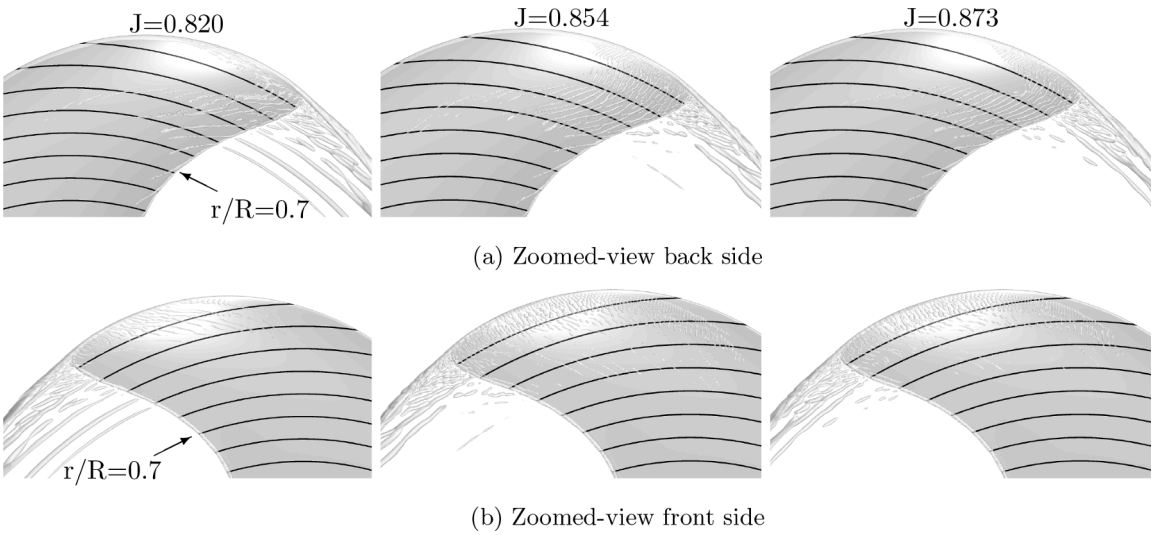

Fig. 9. Distribution of Q-criterion iso-surface = 200 around the blade tip at low J values.

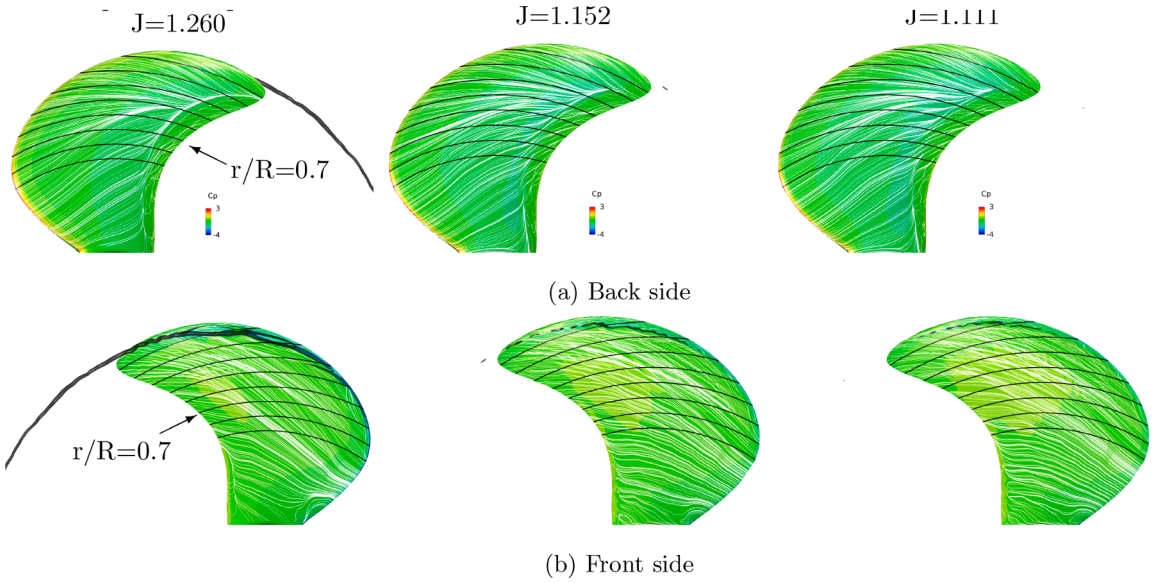

Fig. 10. Flow properties at different front side tip vortex conditions. The blade surface is coloured by C_p distribution, the flow streamlines are presented in white, the tip vortex is presented by the pressure iso-surface equal to $C_p = -2$ coloured in black.

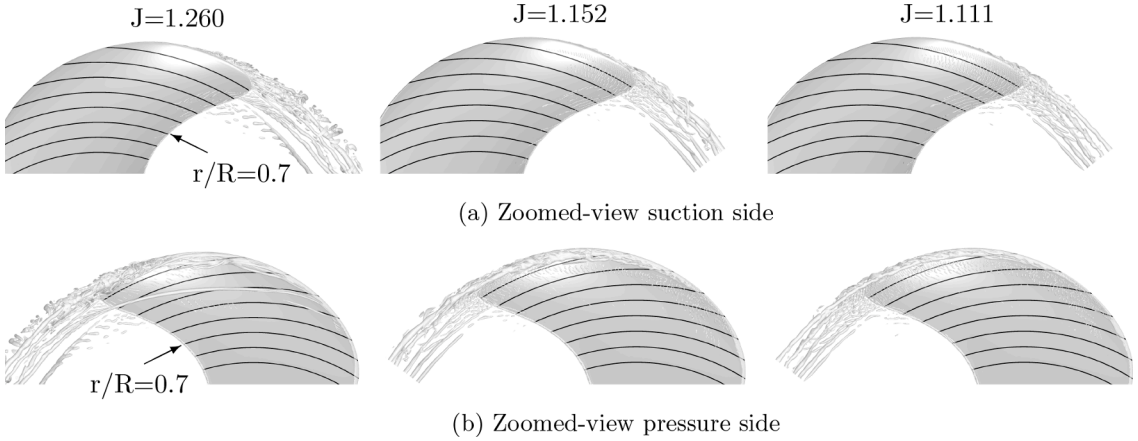

Fig. 11. Distribution of Q-criterion iso-surface = 200 around the blade tip at high J values. The blade surface is divided by $r/R = 0.05$.

Table 3
Variation of thrust, torque, efficiency and TVC inception relative to the smooth propeller condition for different roughness patterns. BS: back side, FS: front side, FR: fully rough.

Case	K_t (%)	K_q (%)	Efficiency (%)	σ_i (%)
Smooth	–	–	–	–
BS tip	− 0.8	0.2	− 1.0	− 16.7
FS tip	1.2	3.8	− 2.5	− 8.5
BS+FS tip	2.1	4.6	− 2.4	− 18.2
FR	− 13.4	3.8	− 16.6	− 22.9

Even though the TVC mitigation of BS+FS tip pattern is higher, the BS tip pattern is selected to be the outcome of the roughness area optimisation for the back side TVC as it has a much lower performance degradation. Modelling of roughness with a wall function has some limitations, especially for the employed wall function where the roughness pattern is included into the CFD with only two representing values, i.e. roughness height and C_s. Including the topology of roughness elements into the computational domain is another alternative where by resolving the flow field around them more flow physics can be captured. These, however, demands for a finer computational resolution around the roughness elements and also an accurate tomography of the roughened area. As the main objective here is to discuss how results of the roughness wall function approach related to the resolving flow field approach, an arbitary roughness tomography is employed that satisfies the same averaged roughness elements height used in the wall function approach, i.e. $K_s = 250$ μm.

In Figs. 13 and 14, numerical results of resolved flow around the roughness elements are presented. The figures are the zoomed view of the blade having the roughness elements on its suction side tip, i.e. the BS tip pattern. The figures include the pressure iso-surface of the saturation pressure colored black, and the vortical structure based on $Q = 1000$ presented with transparent gray color. The low turbulent viscosity around the roughness elements indicates formation of vortical structures around them. The location of these structures are predicted by the curvature correction model, and then the turbulent viscosity is lowered there to allow the flow development. As mentioned earlier, the employed resolution around the roughness elements is limited by the blade tip surface resolution which actually is insufficient to accurately resolve all of the flow structures around the elements. Therefore, its is expected form these results to only provide an estimation on the flow properties which could be expected in the sparse roughness elements application. Vortical structures distribution presented in Fig. 14 shows how flow structures generated by roughness elements interact with each other and the main tip vortices. The figure also includes the pressure iso-surface presented in colored black. The results indicate that depending on the topology of the roughness elements, their location and the propeller working conditions, roughness can increase the risk of bubble or sheet cavitation on the blade. As demonstrated by several research, e.g.

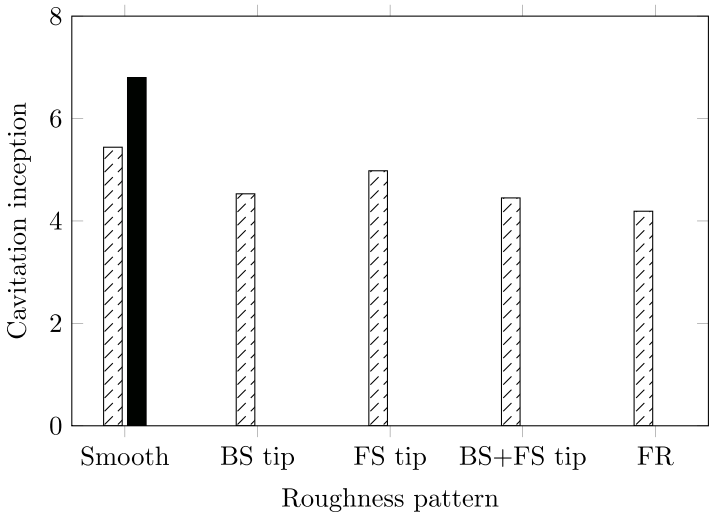

Fig. 12. Variation of the cavitation inception versus different surface roughness areas, solid bar is the extrapolated experimental measurements for the smooth blade. BS: back side, FS: front side, FR: fully rough.

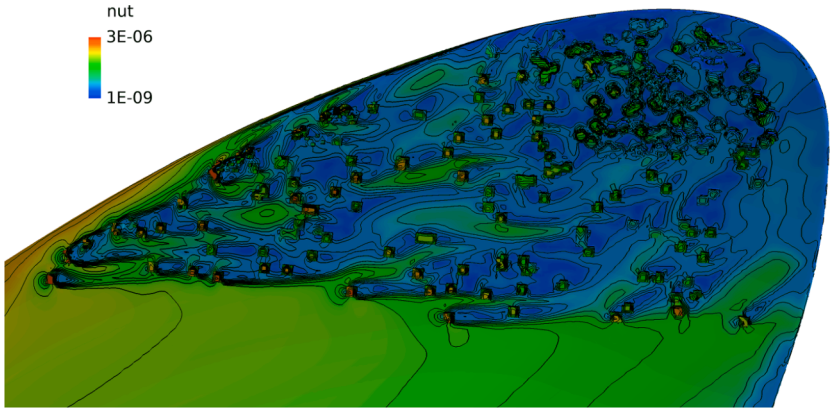

Fig. 13. Distribution of the turbulent viscosity around the roughness elements, zoomed view of the roughness elements for the BS tip roughness pattern.

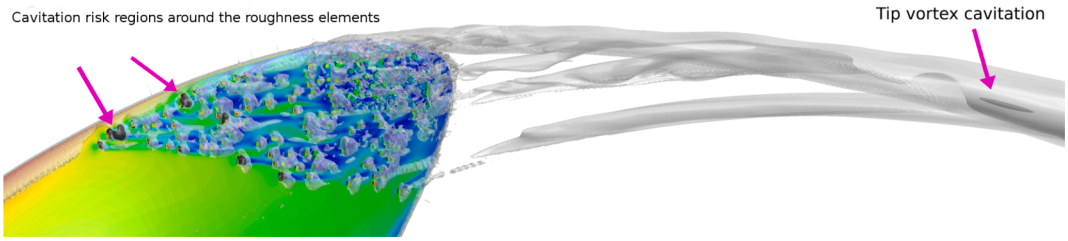

Fig. 14. Distribution of the vortical structures around the roughness elements along with the iso-surface of pressure colored black, zoomed view of the roughness elements for the BS tip roughness pattern.

(Asnaghi et al., 2018a; Cheng et al., 2020a; Liu et al., 2019), formation of cavitation will affect the vorticity distribution through the dilatation term. Especially during the condensation where dilatation leads to a decrease in the magnitude of vorticity. Therefore, one could expect to observe different or generally weaker vortical structures in the cavitating conditions. Thus, the erosiveness analysis of these local low pressure spots around the roughness elements has to remain for future study where the cavitating tip vortex and mass transfer are included modelled.

For the resolved flow around the roughness elements, the cavitation inception is found to be around 3.28 while with wall-modelling approach the predicted inception point is 4.53. Lower propeller performance is noted for the resolved flow as well, Table 4. When conducting a comparative analysis, e.g. comparing different patterns, the large difference between the cavitation inception predictions has less importance. But when it comes to find the balance between the cavitation tip vortex and the blade cavitation, the accurate prediction of flow around roughness elements is inevitable.

4.3. Mitigation of front side TVC

The roughness area optimization of the front side tip vortex is conducted at $J = 1.26$ where more contributions of flow from lower blade radii on the tip vortex formation are observed. The flow structures on the back side are noted to affect the tip vortex properties especially downstream the tip where the trailing vortices interact with the tip vortex. However, it is not clear whether this interaction would affect the tip vortex cavitation inception on the front side of the blade. Therefore, the analysis is started by comparing having roughness all over the front side or back side of the blade, Fig. 15. The results of smooth condition as the reference condition and the fully rough condition as the maximum expected TVC mitigation condition are included.

Very little improvement in TVC mitigation is observed when the roughness is applied on BS of the blade compared to the smooth condition, while the results of FS and FR conditions are found to be similar. This clearly indicates that in order to mitigate the front side TVC, roughness should be applied on the front side. This agrees with our findings from the back side TVC mitigation where it is noted roughness should be applied on the same side of the blade where TVC forms.

In order to find on which radial distance roughness should be applied to effectively mitigate TVC, different radial patterns are considered, e.g. R7080, R8090, R90100 and R70100. These patterns are illustrated in Fig. 4 and described in Table 2. The TVC inception of R7080 pattern is found to be close to the smooth condition results noting very little impact of having roughness on this area on TVC mitigation. Among the tested radial patterns the lowest TVC inception belongs to R70100 where the predicted inception is very close to the results of FS and FR patterns. This indicates the necessity of having roughness in $0.8 < r/R < 1.0$ region in order to practically suppress front side TVC.

Different criteria are tested to narrow down the effective areas on the blade front side in $0.8 < r/R < 1.0$ region. Among the tested criterion, the pressure coefficient is found to be the most effective one. Based on the pressure coefficient distribution close to the blade, different roughness patterns are created, Fig. 4(b). The performance of these patterns relative to the smooth condition is presented in Table 5. The results show in all of the patterns both K_T and K_Q increase compared to the smooth condition. This has led to higher efficiency in these patterns as well. Even though the variation of efficiency is relatively small and can be assumed to lie in the uncertainty of the numerical results, it indicates that none of the patterns would have a negative impact on the propeller performance. As a result, the pattern that has the highest TVC mitigation is selected as the optimum roughness pattern for the front side TVC mitigation, i.e. RE80100.

Table 4
Variation of thrust, torque, efficiency and cavitation inception relative to the smooth foil condition for the BS tip roughness pattern with different modelling approaches.

Case	K_t (%)	K_q (%)	Efficiency (%)	σ_i (%)
Smooth	–	–	–	–
Wall modelled ($y^+ = 35$)	− 0.8	0.2	− 1.0	− 16.7
Roughness resolved ($y^+ = 5$)	− 1.9	0.1	− 1.8	− 38.7

4.4. Optimised roughness pattern

The optimized roughness pattern (ORP) is achieved by the simultaneous consideration of the optimum roughness pattern of the back side tip vortex and the optimum roughness pattern of the front side tip vortex already obtained in the previous sections. This would provide a roughness pattern that can mitigate TVC in a wide range of operations with an overall minimized performance degradation. This ORP consists of the BS Tip pattern and RE80100 pattern, Table 2.

In Fig. 16, the open water performance of the model scale propeller in smooth and ORP is presented. In the presented results, the roughness is modelled via the rough wall function. For $J < 1.125$, similar torque coefficients are predicted in smooth and ORP while the thrust coefficient is lower in the ORP. For larger values of J, the produced thrust in smooth and ORP conditions are similar while more torque is needed in the ORP condition. This leads to having a lower efficiency in ORP condition across all of the operating conditions. Interestingly, the efficiency curves are found to be similar in smooth and ORP conditions with a small shift downward in ORP. In Fig. 17, the cavitation inception diagram of the model scale propeller in smooth and ORP conditions are presented. The general impression is that application of roughness leads to a wider cavitation free bucket on the side, and the impact on the centre area, e.g. $J = 1.05$, is small. This is expected as in $1.0 < J < 1.1$ operating conditions, the dominant TVC switches from one side of the blade to the other one. This corresponds to have a weak TVC and therefore small impact of roughness on its strength. More detailed comparison of TVC mitigation and performance degradation is presented in Fig. 18 for the back side TVC and Fig. 19 for the front side TVC. For the back side tip vortex, the experimental measurements of the roughened propeller are included. It can be noted from the numerical results that the average performance degradation for ORP in back side TVC mitigation is around 1.4% and the average TVC mitigation is 14% where the lowest impact of

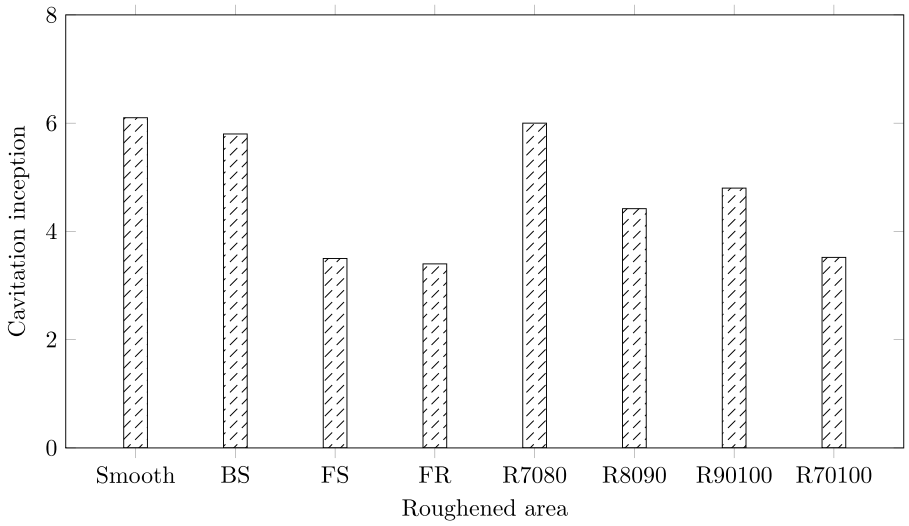

Fig. 15. Variation of the cavitation inception versus different surface roughness areas at $J = 1.26$, FR: fully rough foil, BS: back side roughness, FS: front side roughness, R: radial position of the roughened area on the front side of the blade.

Table 5
Variation of thrust, torque, efficiency and TVC inception relative to the smooth foil condition for different roughness patterns on the front side leading edge at $J = 1.26$, $y^+ = 35$.

Case	K_t (%)	K_q (%)	Efficiency (%)	σ_i (%)
Smooth	–	–	–	–
RE8090	2.21	1.55	0.64	− 22.2
RE90100	4.17	3.37	0.78	− 20.3
RE8595	3.22	2.44	0.75	− 29.1
RE80100	4.8	3.87	0.90	− 35.2

roughness on TVC mitigation is found to be around $J = 0.93$. The experimental measurements show even higher TVC mitigation with an average of 28.5% which comes with the average cost of 2% performance degradation. Both of the numerical results and experimental measurements show the same trend in the TVC mitigation where the maximum mitigation is observed in the highest propeller load, i.e. $J = 0.82$. As mentioned previously, the discrepancy in the results can be related to all of the possible uncertainty in the roughness properties and its application in the numerical simulations and experimental tests.

Compared to ORP results of the back side TVC, the impact of roughness on mitigation and performance degradation is found to be larger in the front side TVC where the average performance degradation is around 1.8% and the average TVC mitigation is 37%. An instance of the experimental observation for the roughness application is presented in Fig. 20. The presented instance is for $\sigma = 2$ at $J = 0.9$ where in the smooth condition a clear cavitating tip vortex forms on the back side of the blade. The applied optimum roughness pattern follows the details presented in Table 2 where only the back side roughness is visible in the

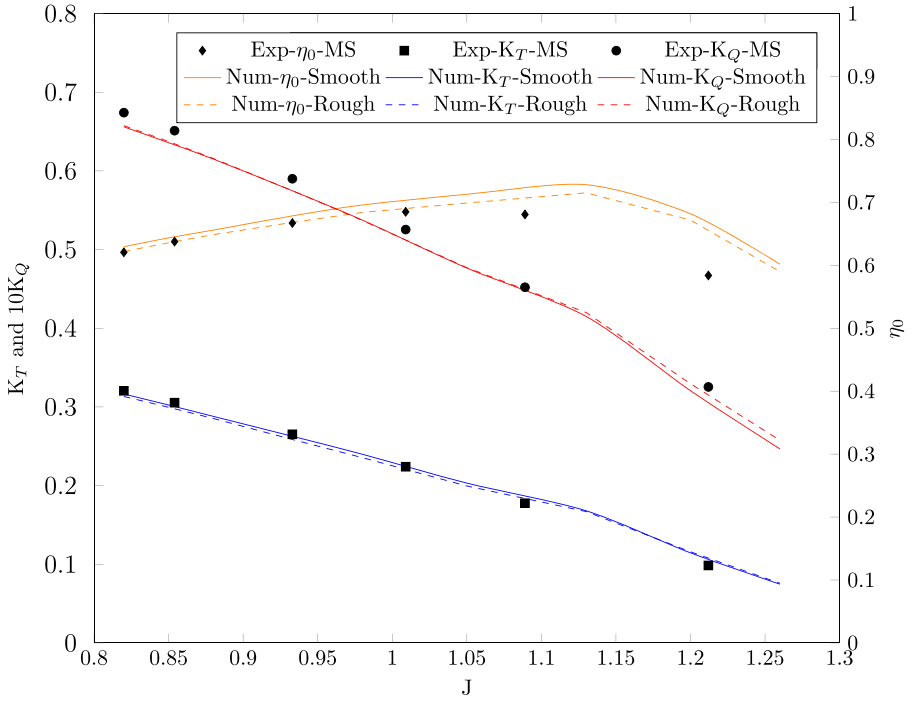

Fig. 16. Comparison of the open water performance of the model scale propeller in the smooth and optimised roughness area conditions, $y^+ = 35$.

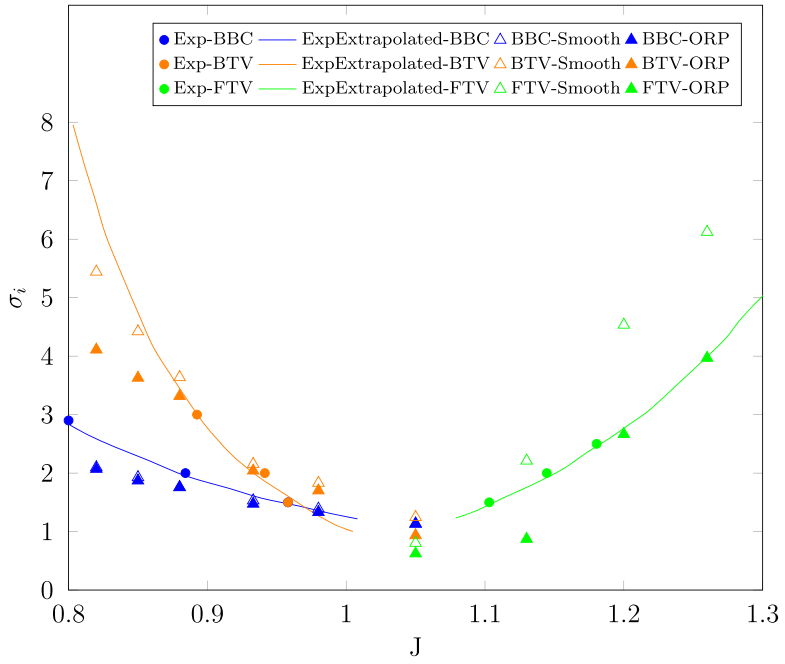

Fig. 17. Comparison of open water cavitation inception diagrams of the smooth and optimised roughness pattern (ORP) conditions for the model scale propeller represented by FTV, front tip vortex; BTV, back tip vortex; and BBC, back bubble cavitation, $y^+ = 35$.

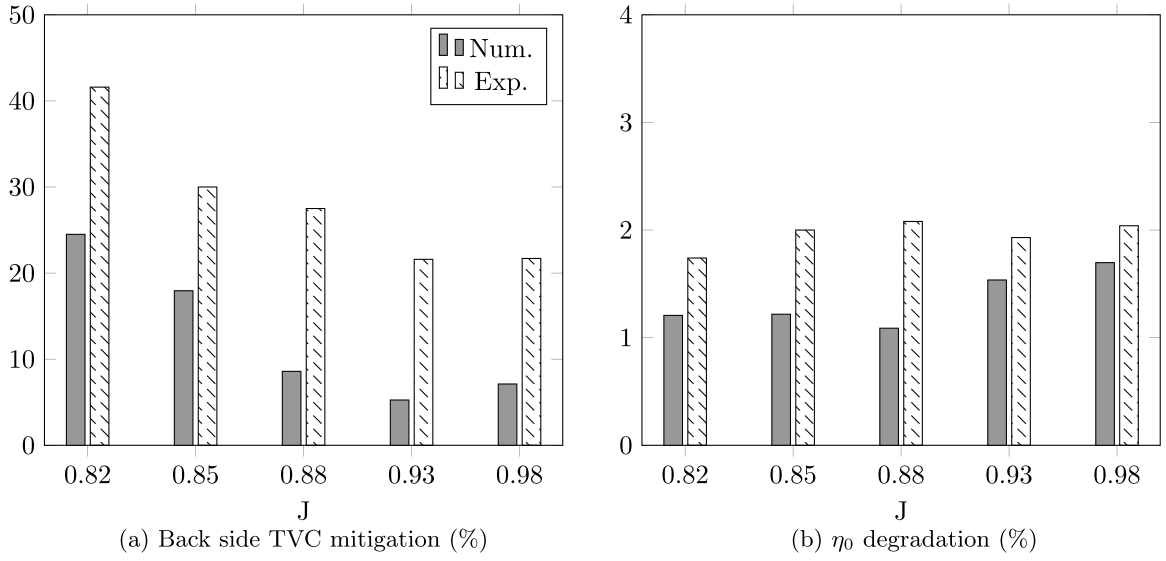

(a) Back side TVC mitigation (%) (b) η_0 degradation (%)

Fig. 18. Percentage of the back side TVC mitigation and open water efficiency drop in different operating conditions for the optimum roughness pattern relative to the smooth propeller condition, $y^+ = 35$.

figure. It can be clearly seen that in the roughened blade, the cavitating tip vortex has been completely disappeared and only small bubbles can be noted around the tip. These bubbles can be either free-stream nuclei caught by the tip vortex structures or the small bubbly cavitation formed around the roughness elements.

4.5. Optimized roughness pattern in full scale condition

In Fig. 21, TVC mitigation and performance degradation of the full scale propeller at three different operating conditions are provided. These simulations are performed on the propeller with $y^+ = 50$ where the roughness elements having $K_s^+ = 925$ are incorporated into the computational domain, Table 1. Similar to the model scale results, the lowest TVC mitigation and highest performance degradation are found to be at the design point, i.e. $J = 0.93$. The results indicate an average TVC mitigation of 22% and performance degradation of 1.4% by employing optimised roughness pattern.

Resolving the flow around the roughness elements provides the possibility of investigating the risk of bubble or sheet cavitation formation at these spots. At the tested conditions, no obvious increase in bubble or sheet cavitation due to the roughness elements is observed. However, further investigation of this analysis remains for future study with models that could evaluate the cavitation erosiveness (Arabnejad, 2020; Arabnejad et al., 2019).

5. Conclusion

The results on the tested propeller in model scale and full scale

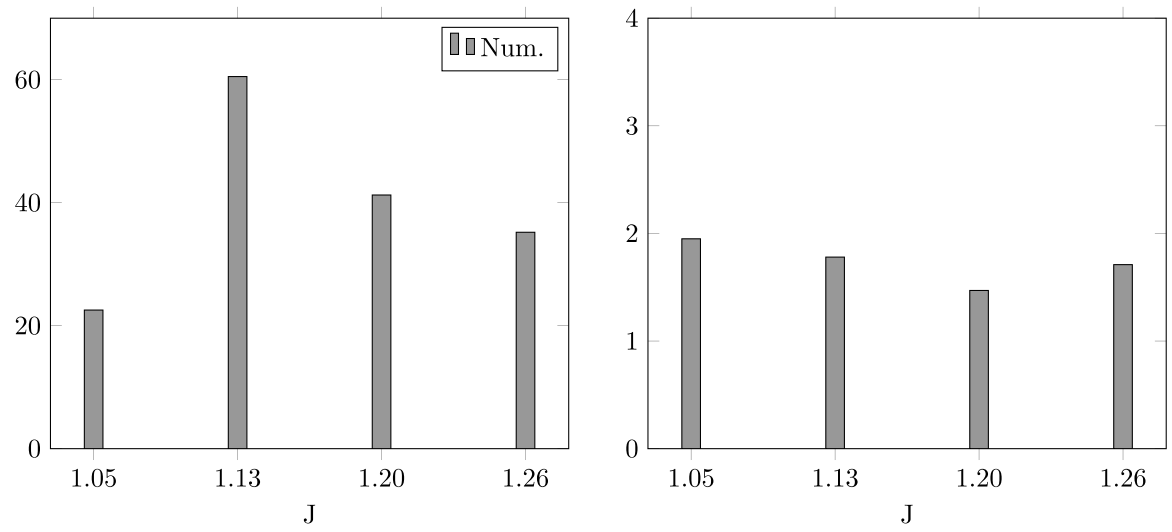

(a) Pressure side TVC mitigation (%) (b) η_0 degradation (%)

Fig. 19. Percentage of the pressure side TVC mitigation and open water efficiency drop in different operating conditions for the optimum roughness pattern, $y^+ = 35$.

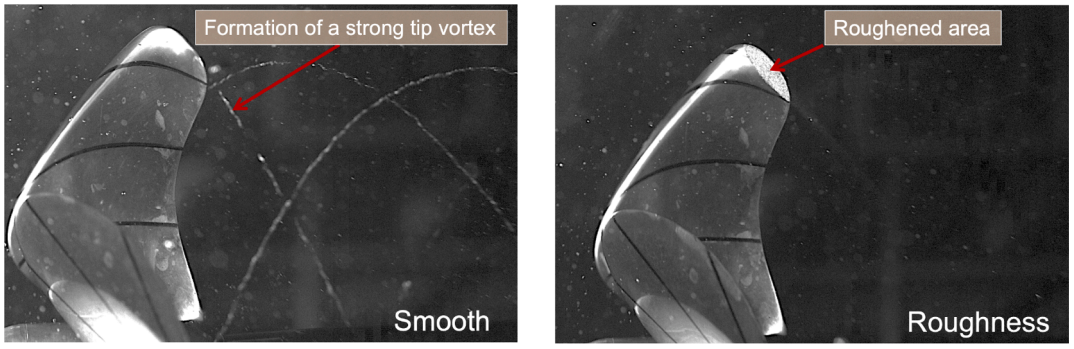

Fig. 20. An instance of cavitating tip vortex flows for the smooth and optimum roughness pattern in the model scale propeller, $\sigma = 2$, $J = 0.9$.

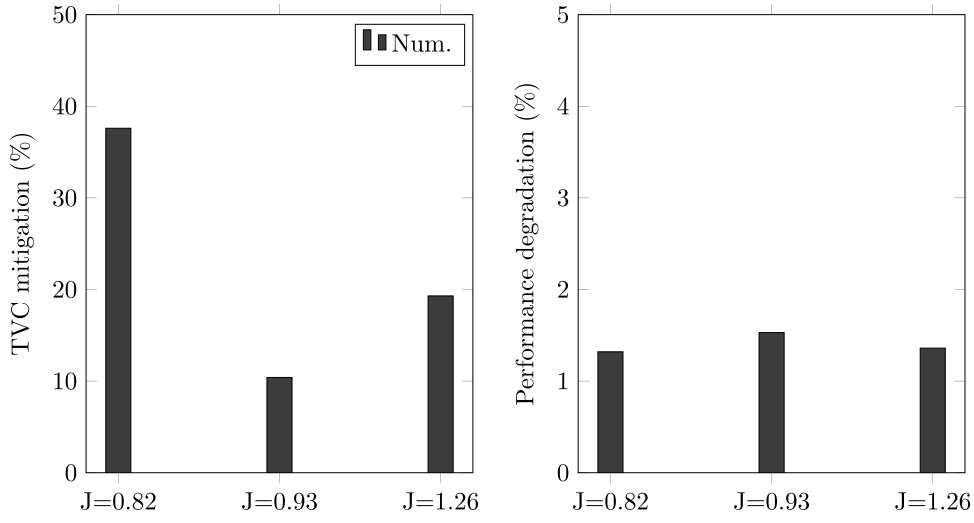

Fig. 21. The optimum roughness area results for the full scale propeller. TVC and propeller performance of each operating condition is normalised by the smooth propeller results of that condition.

conditions show that the application of roughness on a specified and restricted area on the blade can be a solution to improve inception characteristics of a tip vortex while keeping the propeller performance degradation in a reasonable range. Roughness elements interact with the boundary layer developed on the blade and consequently alter its distribution and properties. If the area where the roughness is applied

coincides with the area where the tip vortex forms, this interaction affects the tip vortex formation leading to a less concentrated tip vortex, i.e. tip vortex mitigation.

The negative effects of roughness on the propeller performance can be minimized when the roughness area is optimized based on the flow properties and structures effective in tip vortex formation and development. For the evaluated propeller design, two distinct types of tip vortices are observed. At lower advance ratio numbers, the vortex forms on the tip of the blade which can incept either on the tip or slightly downstream depending on the tip vortex strength dependency on the roll-up process. For this type of tip vortex, application of roughness on the blade tip region where the vortex forms is found to be effective. The other type of tip vortex appears at higher J values as leading edge tip vortex where roughness application on the limited area of leading edge on the same side of the vortex roll-up is found to be effective. The optimized pattern that can be used across different operating conditions are obtained by simultaneous application of roughness on these two areas.

It is noted that application of roughness leads to a wider cavitation free bucket where its impact in the operating conditions close to the design point is lower compared to the conditions with higher loads on the blade. The findings show that the optimized roughness pattern in the model scale condition leads to an average TVC mitigation of 37% with an average performance degradation of 1.8% while in the full scale condition an average TVC mitigation of 22% and performance degradation of 1.4% are obtained

In the obtained results, no obvious indication of increasing the risk of bubble or sheet cavitation around the roughness elements is observed. This agrees well with our previous numerical and experimental investigations on the TVC mitigation around an elliptical foil. There are, however, a few key factors in practical application of roughness for TVC mitigation that demands further considerations and investigations. The free stream turbulence variation, i.e. wake flow effect, or the roughness impact on the cavitating tip vortex conditions are two examples of these key factors. Even though, the numerical results presented in this paper clearly show the capability of roughness application in mitigation of tip vortex flows in both model scale and full scale conditions. We showed if the roughness pattern is optimized with respect to the tip vortex flow properties, a reasonable balance between the TVC mitigation and performance degradation can be achieved.

CRediT authorship contribution statement

Abolfazl Asnaghi: Conceptualization, Methodology, Validation, Formal analysis, Investigation, Writing - original draft. **Urban Svennberg:** Conceptualization, Methodology, Validation, Formal analysis, Investigation, Writing - review & editing. **Robert Gustafsson:** Conceptualization, Methodology, Formal analysis, Investigation. **Rickard E. Bensow:** Conceptualization, Methodology, Formal analysis, Investigation, Writing - review & editing, Supervision, Funding acquisition.

Declaration of Competing Interest

The authors declare that they have no known competing financial interests or personal relationships that could have appeared to influence the work reported in this paper.

Acknowledgements

Financial support for this work has been provided by VINNOVA through the RoughProp project, Grant number 2018-04085, and Kongsberg Maritime Sweden AB through the University Technology Centre in Computational Hydrodynamics hosted at the Department of Mechanics and Maritime Sciences at Chalmers. The simulations are performed on resources at Chalmers Centre for Computational Science and Engineering (C3SE) provided by the Swedish National Infrastructure for Computing (SNIC).

References

Aktas, B., Yilmaz, N., Atlar, M., Sasaki, N., Fitzsimmons, P., Taylor, D., 2019. Suppression of tip vortex cavitation noise using pressurepores technology: a numerical and experimental investigation. Proceedings of Sixth International Symposium on Marine Propulsion, smp 19, Rome, Italy, May.

Arabnejad, M., 2020. Assessment of cavitation erosion risk based on single-fluid simulation of cavitating flows. Ph.D. thesis.

Arabnejad, M., Amini, A., Farhat, M., Bensow, R., 2019. Numerical and experimental investigation of shedding mechanisms from leading-edge cavitation. Int. J. Multiph. Flow 119, 123–143.

Arndt, R., Keller, A., 1992. Water quality effects on cavitation inception in a trailing vortex. J. Fluids Eng. 114, 430–438.

Arndt, R., Pennings, P., Bosschers, J., van Terwisga, T., 2015. The singing vortex. Interface Focus 5 (5). https://doi.org/10.1098/rsfs.2015.0025.

Arolla, S., 2013. Modeling and eddy simulation of rotating and curved turbulent flows. Iowa State University, Ames, Iowa. Doctoral Thesis.

Arolla, S., Durbin, P., 2014. A rotation/curvature correction for turbulence models for applied CFD. Prog. Comput. Fluid Dyn. Int. J. 14 (6), 341–351.

Asnaghi, A., 2018. Computational modelling for cavitation and tip vortex flows. Chalmers University of Technology. Ph.D. thesis.

Asnaghi, A., Feymark, A., Bensow, R., 2015. Computational analysis of cavitating marine propeller performance using OpenFOAM. Fourth International Symposium on Marine Propulsors, At Austin, Texas, USA.

Asnaghi, A., Feymark, A., Bensow, R., 2018. Numerical investigation of the impact of computational resolution on shedding cavity structures. Int. J. Multiph. Flow 107, 33–50.

Asnaghi, A., Svennberg, U., Bensow, R., 2018. Numerical and experimental analysis of cavitation inception behaviour for high-skewed low-noise propellers. Appl. Ocean Res. 79, 197–214.

Asnaghi, A., Svennberg, U., Bensow, R., 2019. Evaluation of curvature correction methods for tip vortex prediction in SST k turbulence model framework. Int. J. Heat Fluid Flow 75, 135–152.

Asnaghi, A., Svennberg, U., Bensow, R., 2020. Large eddy simulations of cavitating tip vortex flows. Ocean Eng. 195, 106703.

Asnaghi, A., Svennberg, U., Gustaffson, R., Bensow, R., 2020. Investigations of tip vortex mitigation by using roughness. Phys. Fluids 32, (065111)1–17.

Asnaghi, A., Svennberg, U., Gustafsson, R., Bensow, R., 2019. Propeller tip vortex cavitation mitigation using roughness. Proceedings of VIII International Conference on Computational Methods in Marine Engineering, MARINE 2019, Gothenburg, Sweden.

Asnaghi, A., Svennberg, U., Gustafsson, R., Bensow, R., 2019. Roughness effects on the tip vortex strength and cavitation inception. Proceedings of Sixth International Symposium on Marine Propulsion, smp 19, Rome, Italy, May.

Bensow, R., 2011. Simulation of the unsteady cavitation on the Delft Twist11 foil using RANS, DES and LES. In Proceedings of the 2nd International Symposium on Marine Propulsors. Hamburg, Germany.

Bensow, R., Bark, G., 2010. Simulating cavitating flows with LES in OpenFOAM. V European Conference on Computational Fluid Dynamics, ECCOMAS CFD, Lisbon, Portugal.

Bosschers, J., 2018. Propeller tip-vortex cavitation and its broadband noise. University of Twente. Ph.D. thesis.

Boulon, O., Franc, J., Michel, J., 1997. Tip vortex cavitation on an oscillating hydrofoil. J. Fluids Eng. Trans. ASME 119 (4), 752–758.

Brianon-Marjollet, L., Merle, L., 1997. Inception, development, and noise of a tip vortex cavitation. Twenty-First Symposium on Naval Hydrodynamics. Washington, DC.

Brown, M., Schroeder, S., Balaras, E., 2015. Vortex structure characterization of tip loaded propellers. Fourth International Symposium on Marine Propulsors smp15, Austin, Texas, USA, June.

Chahine, G., Frederick, G., Bateman, R., 1993. Propeller tip vortex cavitation suppression using selective polymer injection. J. Fluids Eng. Trans. ASME 115 (3), 497–503.

Chang, N., Ganesh, H., Yakushiji, R., Ceccio, S., 2011. Tip vortex cavitation suppression by active mass injection. J. Fluids Eng. 133, 111301 (11 pages).

Cheng, H., Bai, X., Long, X., Ji, B., Peng, X., Farhat, M., 2020. Large eddy simulation of the tip-leakage cavitating flow with an insight on how cavitation influences vorticity and turbulence. Appl. Math. Model. 77, 788–809.

Cheng, H., Long, X., Ji, B., Peng, X., Farhat, M., 2021. A new euler-lagrangian cavitation model for tip-vortex cavitation with the effect of non-condensable gas. Int. J. Multiph. Flow 134, 103441.

Dreyer, M., 2015. Mind The Gap: Tip Leakage Vortex Dynamics and Cavitation in Axial Turbines. Ecole Polytechnique Federale De Lausanne. Ph.D. thesis.

Felli, M., Falchi, M., 2011. Propeller tip and hub vortex dynamics in the interaction with a rudder. Exp. Fluids 51 (5), 1385–1402.

Fruman, D., Aflalo, S., 1989. Tip vortex cavitation inhibition by drag-reducing polymer solutions. J. Fluids Eng. Trans ASME 111 (2), 211–216.

Ghahramani, E., 2020. Numerical simulation and analysis of multi-scale cavitating flows using a hybrid mixture-bubble model. Chalmers University of Technology. Ph.D. thesis.

Ghahramani, E., Arabnejad, M., Bensow, R., 2019. A comparative study between numerical methods in simulation of cavitating bubbles. Int. J. Multiph. Flow 111, 339–359.

Gim, O., Lee, G., 2013. Flow characteristics and tip vortex formation around a NACA0018 foil with an endplate. Ocean Eng. 60, 28–40.
Han, Y., Tan, L., 2019. Spatial temporal evolution of tip leakage vortex in a mixed-flow pump with tip clearance. J. Fluids Eng. Trans. ASME 141 (8).(081302)1–11
Han, Y., Tan, L., 2020. Dynamic mode decomposition and reconstruction of tip leakage vortex in a mixed flow pump as turbine at pump mode. Renew. Energy 155, 725–734.
Higuchi, H., Arndt, R., Rogers, M., 1989. Characteristics of tip vortex cavitation noise. J. Fluids Eng. Trans. ASME 111 (4), 495–501.
Hsu, C., 1991. Studies of scaling of tip vortex cavitation inception on marine lifting surfaces. J. Fluids Eng. Trans. ASME 113 (3), 504–508.
Hunt, J., Wray, A., Moin, P., 1998. Eddies, stream, and convergence zones in turbulent flows. Center for Turbulence Research Report CTR-S88.
Johnsson, C.A., Ruttgerson, O., 1991. Leading edge roughness: a way to improve propeller tip vortex cavitation. Propeller Shafting Symposium.
Kolar, V., 2007. Vortex identification: new requirements and limitations. Int. J. Heat Fluid 28, 638–652.
Korkut, E., Atlar, M., 2002. On the importance of the effect of turbulence in cavitation inception tests of marine propellers. Proc. R. Soc. Lond. A 458 (2017), 29–48.
Kruger, C., Kornev, N., Greitsch, L., 2016. Influence of propeller tip roughness on tip vortex strength and propeller performance. Ship Technol. Res. 63 (2), 110–120.
Kuiper, G., 1981. Cavitation inception on ship propeller models. Delft University of Technology. Ph.D. thesis.
Kuiper, G., 2001b2001. New developments around sheet and tip vortex cavitation on ships propellers. CAV 2001: Fourth International Symposium on Cavitation, June 20–23, 2001, California Institute of Technology, Pasadena, CA USA..
Ligneul, P., Latorre, R., 1993. Study of nuclei distribution and vortex diffusion influence on nuclei capture by a tip vortex and nuclei capture noise. J. Fluids Eng. Trans. ASME 115 (3), 504–507.
Liu, M., Tan, L., Cao, S., 2019. Cavitation vortex turbulence interaction and one-dimensional model prediction of pressure for hydrofoil ale15 by large eddy simulation. J. Fluids Eng. Trans. ASME 141 (2).(021103)1–17
Long, Y., Han, C., Ji, B., Long, X., Wang, Y., 2020. Verification and validation of large eddy simulations of turbulent cavitating flow around two marine propellers with emphasis on the skew angle effects. Appl. Ocean Res. 101, 102167.
Lu, N., Bensow, R., Bark, G., 2014. Large eddy simulation of cavitation development on highly skewed propellers. J. Mar. Sci. Technol. (Japan) 19 (2). https://doi.org/10.1007/s00773-013-0240-3.
Maines, B., Arndt, R., 1997. The case of the singing vortex. J. Fluids Eng. Trans. ASME 119 (2), 271–276.
OpenFoam:, The Open Source CFD Toolbox openfoam foundation. http://www.openfoam.com Accessed: 2015-10-14.
Park, S., Lee, S., You, G., Suh, J., 2014. An experimental study on tip vortex cavitation suppression in a marine propeller. J. Ship Res. 58 (2), 1–11.
Peng, X., Wang, B., Li, H., Xu, L., Song, M., 2017. Generation of abnormal acoustic noise: Singing of a cavitating tip vortex. Phys. Rev. Fluids 2, 053602.
Peng, X., Xu, L., Song, M., Cao, Y., 2015. Vortex singing in tip vortex cavitation under the effect of water quality. J. Phys. 656 (1), 012185.
Pennings, P., Westerweel, J., Van Terwisga, T., 2015. Sound signature of propeller tip vortex cavitation. J. Phys. 656 (1), 012186.
Pereira, F., Di Felice, F., Salvatore, F., 2016. Propeller cavitation in non-uniform flow and correlation with the near pressure field. J. Mar. Sci. Eng. 4 (4), 1–13.
Rivetti, A., Angulo, M., Lucino, C., Liscia, S., 2014. Mitigation of tip vortex cavitation by means of air injection on a Kaplan turbine scale model. IOP Conference Series: Earth and Environmental Science, 22.
Ryo, Y., 2009. Mechanism of Tip Vortex Cavitation Suppression by Polymer and Water Injection. Naval Architecture and Marine Engineering, University of Michigan, Horace H. Rackham School of Graduate Studies.
Sezen, S., Dogrul, A., BAL, S., 2016. Tip vortex index (TVI) technique for inboard propeller noise estimation. 1st International Congress on Ship and Marine Technology, At Piri Reis University, Tuzla, Istanbu.
Shin, K., Andersen, P., 2015. CFD analysis of cloud cavitation on three tip-modified propellers with systematically varied tip geometry. J. Phys. 656 (1), 012139.
Souders, W., Platzer, G., 1981. Tip Vortex Cavitation Characteristics and Delay of Inception on a Three-Dimensional Hydrofoil. Naval Ship Research and Development Center,.
StarCCM, -user guide, version 10.06. https://www.cd-adapco.com/ Accessed: 2017-3-10.
Tapia, X., 2009. Modelling of wind flow over complex terrain using OpenFoam. University of Gavle. Master thesis.
Wallin, S., Johansson, A., 2002. Modelling streamline curvature effects in explicit algebraic Reynolds stress turbulence models. Int. J. Heat Fluid Flow 23 (5), 721–730.